formate (*5*, *18*, *35*) or another key precursor (*37*) at Zn-decorated Cu sites.

Moreover, the present model also consistently explains other dynamical effects reported on methanol catalysts. For example, shape changes observed for Cu NPs on a ZnO support were observed by in situ extended x-ray absorption fine structure and in situ TEM (*6*, *7*, *9*). In the present model, the Zn atoms incorporated into the Cu surface under reducing conditions result in a decrease in the surface energy of Cu, and this will, according to (*7*), contribute to the increased wetting of Cu NPs on ZnO and provides an explanation of transient activity profiles.

REFERENCES AND NOTES

1. R. Schlögl, *Angew. Chem. Int. Ed.* **54**, 3465–3520 (2015).
2. K. Honkala *et al.*, *Science* **307**, 555–558 (2005).
3. G. A. Olah, *Angew. Chem. Int. Ed.* **52**, 104–107 (2013).
4. J. B. Hansen, P. E. Højlund Nielsen, in *Handbook of Heterogeneous Catalysis*, G. Ertl, H. Knözinger, F. Schüth, J. Weitkamp, Eds. (Wiley-VCH, Weinheim, Germany, ed. 2, 2008), pp. 2920–2949.
5. M. Behrens *et al.*, *Science* **336**, 893–897 (2012).
6. P. L. Hansen *et al.*, *Science* **295**, 2053–2055 (2002).
7. P. C. K. Vesborg *et al.*, *J. Catal.* **262**, 65–72 (2009).
8. M. Muhler, E. Törnqvist, L. P. Nielsen, B. S. Clausen, H. Topsøe, *Catal. Lett.* **25**, 1–10 (1994).
9. J.-D. Grunwaldt, A. M. Molenbroek, N.-Y. Topsøe, H. Topsøe, B. S. Clausen, *J. Catal.* **194**, 452–460 (2000).
10. R. Naumann d'Alnoncourt *et al.*, *Phys. Chem. Chem. Phys.* **8**, 1525–1538 (2006).
11. S. Kuld, C. Conradsen, P. G. Moses, I. Chorkendorff, J. Sehested, *Angew. Chem. Int. Ed.* **53**, 5941–5945 (2014).
12. J. Graciani *et al.*, *Science* **345**, 546–550 (2014).
13. J. Nakamura, I. Nakamura, T. Uchijima, T. Watanabe, T. Fujitani, *Stud. Surf. Sci. Catal.* **101B**, 1389–1399 (1996).
14. J. Schumann *et al.*, *ACS Catal.* **5**, 3260–3270 (2015).
15. J. Nakamura, Y. Choi, T. Fujitani, *Top. Catal.* **22**, 277–285 (2003).
16. M. Kurtz *et al.*, *Catal. Lett.* **92**, 49–52 (2004).
17. F. Liao *et al.*, *Angew. Chem. Int. Ed.* **50**, 2162–2165 (2011).
18. F. Studt *et al.*, *Chem. Cat. Chem.* **7**, 1105–1111 (2015).
19. E. D. Batyrev, J. C. van den Heuvel, J. Beckers, W. P. A. Jansen, H. L. Castricum, *J. Catal.* **229**, 136–143 (2005).
20. W. P. A. Jansen *et al.*, *J. Catal.* **210**, 229–236 (2002).
21. T. Lunkenbein, J. Schumann, M. Behrens, R. Schlögl, M. G. Willinger, *Angew. Chem. Int. Ed.* **54**, 4544–4548 (2015).
22. I. Kasatkin, P. Kurr, B. Kniep, A. Trunschke, R. Schlögl, *Angew. Chem. Int. Ed.* **119**, 7465–7468 (2007).
23. M. S. Spencer, *Surf. Sci.* **192**, 336–343 (1987).
24. J. Yoshihara, C. T. Campbell, *J. Catal.* **161**, 776–782 (1996).
25. I. Barin, *Thermodynamic Data of Pure Substances* (Weinheim, Basel, Switzerland; Cambridge, New York, VCH, 1989).
26. E. J. Rapperport, J. P. Pemsler, *Metall. Trans.* **3**, 827–831 (1972).
27. M. S. Spencer, *Surf. Sci.* **192**, 329–335 (1987).
28. R. Ouyang, J.-X. Liu, W.-X. Li, *J. Am. Chem. Soc.* **135**, 1760–1771 (2013).
29. D. B. Rasmussen *et al.*, *J. Catal.* **293**, 205–214 (2012).
30. L. Vitos, A. V. Ruban, H. L. Skriver, J. Kollár, *Surf. Sci.* **411**, 186–202 (1998).
31. M. Sano, T. Adaniya, T. Fujitani, J. Nakamura, *J. Phys. Chem.* **106**, 7627–7633 (2002).
32. R. Van Hardeveld, F. Hartog, *Surf. Sci.* **15**, 189–230 (1969).
33. O. Martin, J. Pérez-Ramírez, *Catal. Sci. Technol.* **3**, 3343–3352 (2013).
34. I. A. Fisher, A. T. Bell, *J. Catal.* **184**, 357–376 (1999).
35. W. J. van Rensburg, M. A. Petersen, M. S. Datt, J.-A. van den Berg, P. van Helden, *Catal. Lett.* **145**, 559–568 (2015).
36. L. C. Grabow, M. Mavrikakis, *ACS Catal.* **1**, 365–384 (2011).
37. Y. Yang, D. Mei, C. H. F. Peden, C. T. Campbell, C. A. Mims, *ACS Catal.* **5**, 7328–7337 (2015).
38. G. C. Chinchen, K. C. Waugh, D. A. Whan, *Appl. Catal.* **25**, 101–107 (1986).
39. Y. Yang, C. A. Mims, D. H. Mei, C. H. F. Peden, C. T. Campbell, *J. Catal.* **298**, 10–17 (2013).
40. M. B. Fichtl *et al.*, *Appl. Catal. A.* **502**, 262–270 (2015).
41. M. Kurtz, H. Wilmer, T. Genger, O. Hinrichsen, M. Muhler, *Catal. Lett.* **86**, 77–80 (2003).

ACKNOWLEDGMENTS

We thank P. G. Moses for fruitful discussions and commenting on the work at an early stage. The Center for Individual Nanoparticle Funtionality is sponsored by the Danish National Research Foundation (DNRF54).

SUPPLEMENTARY MATERIALS

www.sciencemag.org/content/352/6288/969/suppl/DC1
Materials and Methods
Figs. S1 to S7
Tables S1 to S8
References (*42*–*49*)

15 December 2015; accepted 15 April 2016
10.1126/science.aaf0718

CATALYSIS

Self-assembly of noble metal monolayers on transition metal carbide nanoparticle catalysts

Sean T. Hunt,[1] Maria Milina,[1] Ana C. Alba-Rubio,[2]* Christopher H. Hendon,[1] James A. Dumesic,[2] Yuriy Román-Leshkov[1]†

We demonstrated the self-assembly of transition metal carbide nanoparticles coated with atomically thin noble metal monolayers by carburizing mixtures of noble metal salts and transition metal oxides encapsulated in removable silica templates. This approach allows for control of the final core-shell architecture, including particle size, monolayer coverage, and heterometallic composition. Carbon-supported $Ti_{0.1}W_{0.9}C$ nanoparticles coated with Pt or bimetallic PtRu monolayers exhibited enhanced resistance to sintering and CO poisoning, achieving an order of magnitude increase in specific activity over commercial catalysts for methanol electrooxidation after 10,000 cycles. These core-shell materials provide a new direction to reduce the loading, enhance the activity, and increase the stability of noble metal catalysts.

Noble metal (NM) catalysts critically enable many existing and emerging technologies, such as catalytic converters (*1*), reforming (*2*), and fuel cells (*3*). However, their scarcity and high cost necessitate the development of catalytic systems with reduced NM loadings, increased activity, and improved durability. In this respect, various nanostructured architectures have been investigated, including atomically dispersed NM catalysts (*4*), hollow nanocages (*5*, *6*), alloyed nanoparticles (NPs) (*7*), and core-shell structures (*8*, *9*). In particular, core-shell NPs composed of an earth-abundant core coated with an atomically thin NM shell are a promising platform that offers both design flexibility and reduced precious-metal loadings. However, achieving independent control over the particle size, core composition, shell composition, and shell thickness poses a substantial challenge (*8*, *9*). State-of-the-art synthetic methods are predominantly limited to a few earth-abundant metallic cores (e.g., Fe, Co, Ni, and Cu) that allow for more precise synthetic control; however, these metal cores form intrinsically metastable core-shell particles that restructure during heating (*10*–*12*) or electrochemical cycling (*13*, *14*).

Early transition metal carbides (TMCs) are earth-abundant ceramics with ideal topochemical properties for supporting precious-metal shells (*15*–*17*). First, TMCs exhibit metallic electrical conductivity, corrosion resistance, and high melting points (*18*). Second, precious metals tend to bind strongly to metal-terminated early TMC surfaces (fig. S1) but cannot readily form stable carbides (*19*). Thus, NMs should coat TMC surfaces but should not alloy with the underlying core. In particular, tungsten carbide (WC) is inexpensive (fig. S2), exhibits a "platinum-like" density of electronic states (*20*, *21*), and its metal-terminated surface forms interfacial Pt-WC bonds that are ~90 kJ mol^{-1} stronger than interfacial Pt-Pt bonds (fig. S1). Although experimental studies on model thin-film systems have corroborated these attractive properties (*15*, *22*, *23*), synthetic efforts to date have not achieved TMC NPs coated with NM monolayers. Until recently, TMC NPs alone were difficult to engineer with controlled properties because their synthesis requires high temperatures (above ~700°C), followed by passivation with dilute oxygen (*24*). Without proper synthetic control, these conditions result in sintered TMC particles covered in both graphitic coke and an oxide surface layer. Such surface impurities preclude core-shell formation because of the unfavorable binding energies between precious metals and contaminated TMC surfaces (fig. S1).

We present here a high-temperature self-assembly method to synthesize size-tunable TMC NPs (<10 nm) coated with monometallic or heterometallic NM surface shells of controlled thicknesses ranging from submonolayer to multilayer coverages. These core-shell materials achieve

[1]Department of Chemical Engineering, Massachusetts Institute of Technology (MIT), Cambridge, MA 02139, USA. [2]Department of Chemical and Biological Engineering, University of Wisconsin–Madison, Madison, WI 53706, USA. *Present address: Department of Chemical and Environmental Engineering, University of Toledo, Toledo, OH 43606, USA. †Corresponding author. Email: yroman@mit.edu

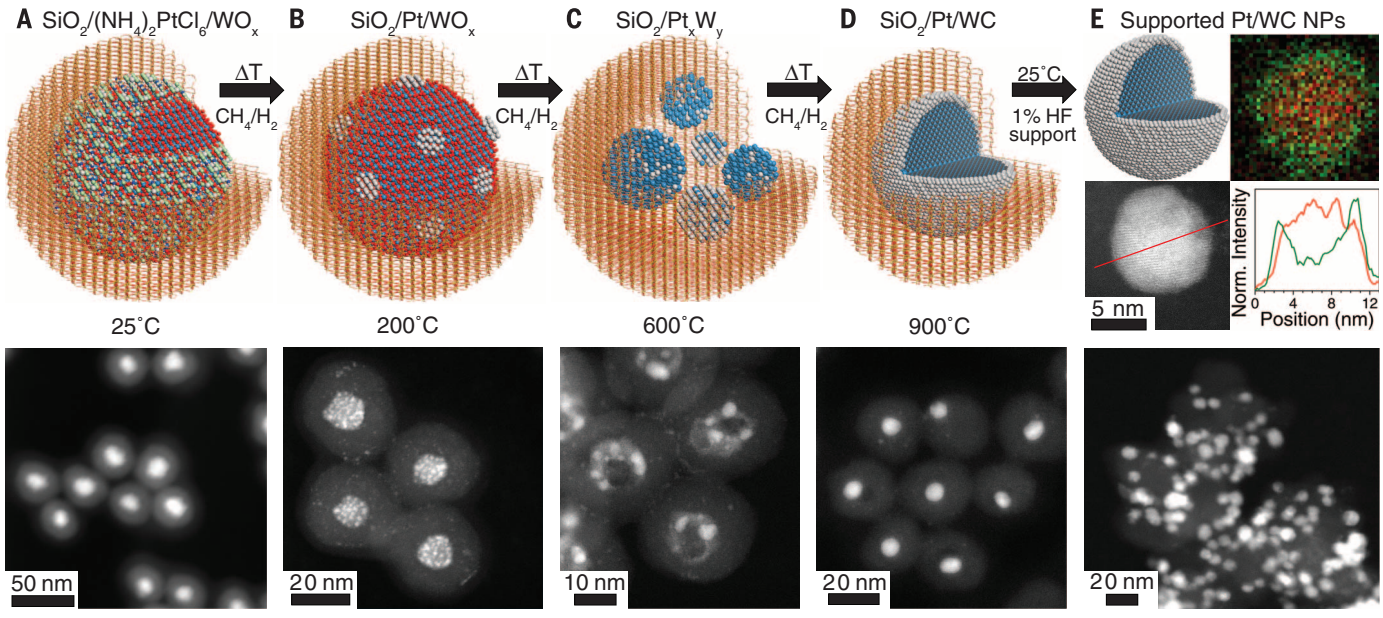

Fig. 1. High-temperature self-assembly of NM monolayers on TMC cores. (**A** to **D**) Schematic representations and corresponding STEM images of (A) silica-encapsulated $(NH_4)_2PtCl_6/WO_x$ NPs synthesized in a one-pot reactor at room temperature and subsequently heated to (B) 200°C, (C) 600°C, and (D) 900°C in a CH_4/H_2 atmosphere. ΔT, temperature change. (**E**) STEM image, EDX map, and line scan (Pt signal in green, W signal in red) of a resulting core-shell Pt/WC NP and a STEM image of Pt/WC formulated on a carbon black support after silica removal.

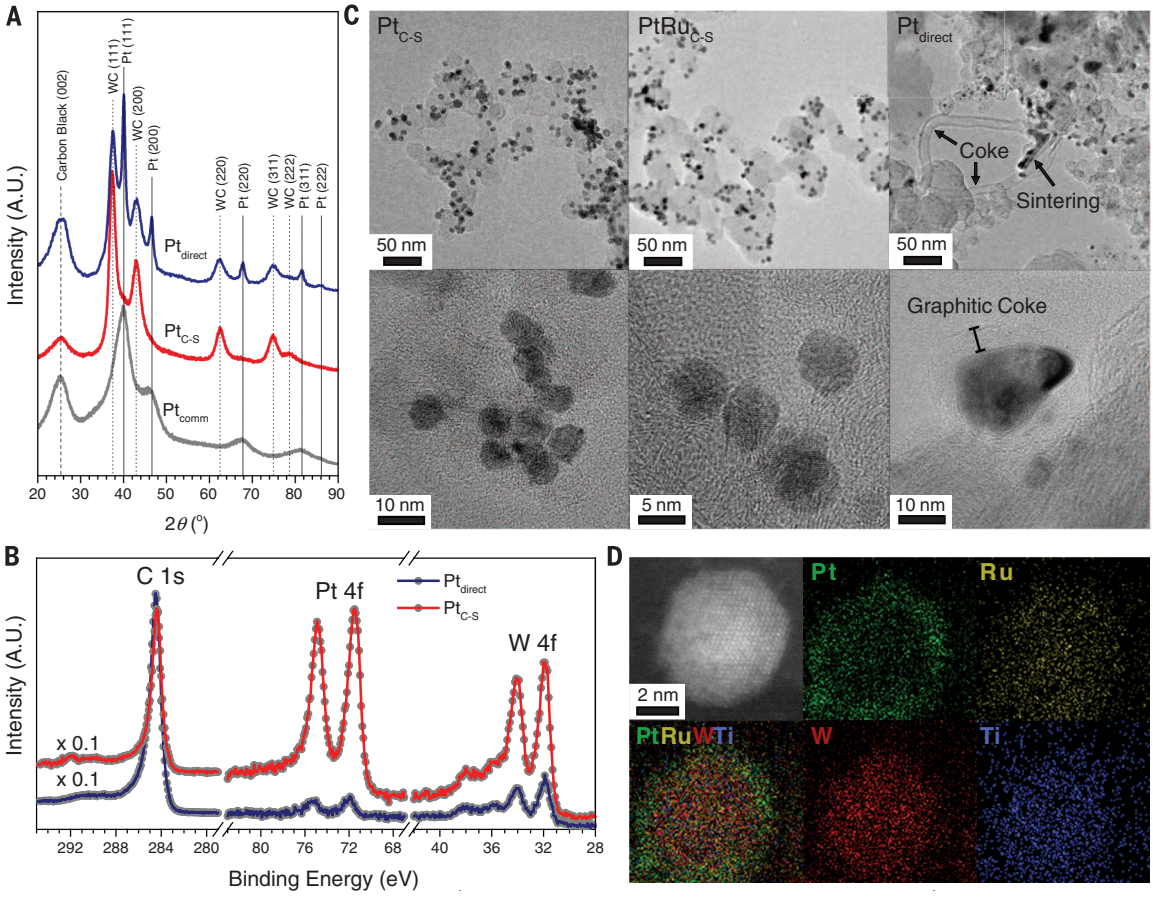

Fig. 2. Experimental corroboration of core-shell structure. (**A**) PXRD diffractograms of Pt_{C-S} and Pt_{direct} compared to Pt_{comm}. A.U., arbitrary units. (**B**) XPS comparison of the C 1s, Pt 4f, and W 4f signals of Pt_{C-S} and Pt_{direct}. (**C**) TEM images of Pt_{C-S}, $PtRu_{C-S}$, and Pt_{direct}. (**D**) STEM and EDX maps of $PtRu_{C-S}$.

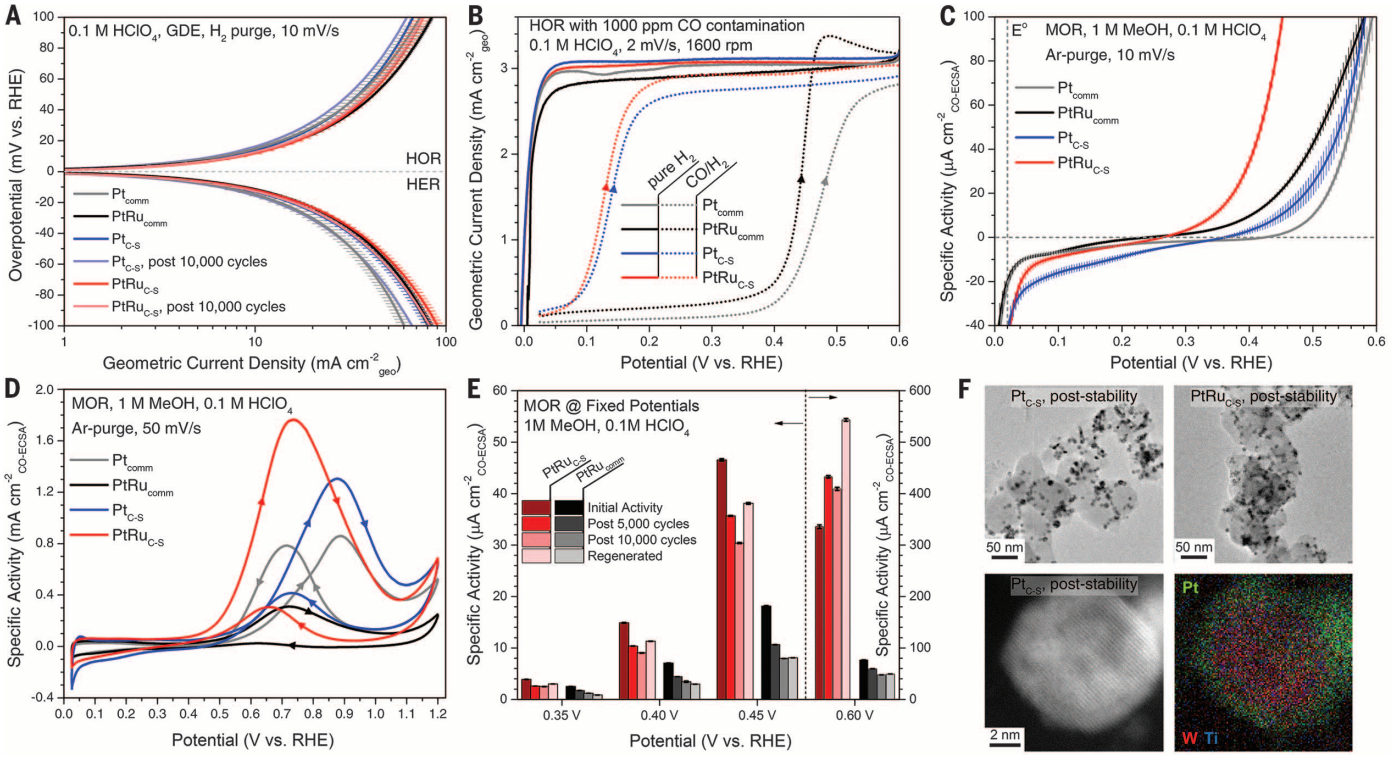

Fig. 3. Electrochemical activity and stability of $Pt_{C\text{-}S}$ and $PtRu_{C\text{-}S}$ compared to commercial catalysts. (**A**) HOR/HER Tafel plots. RHE, reversible hydrogen electrode. (**B**) HOR LSVs with and without CO contamination. (**C**) LSVs and (**D**) CVs for MOR normalized by CO-ECSA roughness factors. (**E**) Steady-state specific activity at fixed potentials after stability cycling and regeneration in alkaline media. (**F**) TEM images of $Pt_{C\text{-}S}$ and $PtRu_{C\text{-}S}$ and a STEM image with EDX map of a $Pt_{C\text{-}S}$ NP after stability cycling.

superior catalytic activity, improved stability, and reduced NM loadings as compared to state-of-the-art commercial catalysts for electrochemical applications. They are also sinter-resistant, and the core-shell structure remains stable at high temperatures under various atmospheres.

Aberration-corrected scanning transmission electron microscopy (STEM) images (Fig. 1) depict the stages of the NM/TMC (shell/core) self-assembly process as a function of temperature, with Pt/WC NP formation as the representative example. In the first step, WO_x NPs were impregnated uniformly with a $(NH_4)_2PtCl_6$ salt and encapsulated in silica nanospheres via a room-temperature reverse microemulsion (RME) (Fig. 1A). This method generated $SiO_2/(NH_4)_2PtCl_6/WO_x$ composites with controlled NP size and Pt loading [see the supporting materials for comprehensive synthetic details (*25*)].

The $SiO_2/(NH_4)_2PtCl_6/WO_x$ composites were then subjected to a temperature ramp under a 15% CH_4/85% H_2 flow (Fig. 1, B to D). At temperatures lower than 200°C, H_2 permeated through the silica nanospheres (*24*), reducing the encapsulated Pt salt into Pt nanoclusters over the WO_x domains (Fig. 1B and fig. S3). By 600°C, the central WO_x NPs underwent reduction, forming metallic mixtures of Pt and W that were trapped within the silica nanospheres (Fig. 1C and figs. S3 and S4). Near 900°C, these small metallic clusters sintered to form single central NPs, while C from methane decomposition intercalated into the W-rich domains, forming WC (Fig. 1D). Because NMs are insoluble in TMC lattices, Pt phase-segregates from the WC domains and wets the central carbide core as an atomically thin shell, resulting in the self-assembly of uniform core-shell NPs as determined by an energy-dispersive x-ray spectroscopy (EDX) map and line scan (Fig. 1E). The silica template was dissolved, and the resulting NPs could then be dispersed in solution with or without a capping agent (fig. S5) or onto a high-surface-area matrix (Fig. 1E). The final Pt/WC particle size and Pt shell thickness were controlled by engineering the WO_x NP size and $(NH_4)_2PtCl_6$ loading in the RME before silica encapsulation and carburization.

Silica encapsulation is critical for controlling core-shell NP formation. In Fig. 2, A to C, we compare two carbon-supported NM/TMC materials, one with silica encapsulation [denoted as $Pt_{C\text{-}S}$, 28%Pt/72%$Ti_{0.1}W_{0.9}C$ supported at 28 weight % (wt%)], and the other without silica encapsulation (denoted as Pt_{direct}, 20%Pt/80% $Ti_{0.1}W_{0.9}C$ supported at 20 wt%). Because TiC is the most electrochemically stable carbide (*26*), a bimetallic TiWC core was used to enhance stability without affecting the WC lattice parameter by more than 1%. The powder x-ray diffraction (PXRD) pattern for $Pt_{C\text{-}S}$ shows reflections consistent with phase-pure face-centered cubic (fcc) WC [powder diffraction file (PDF) no. 00-020-1316] without additional fcc Pt reflections (PDF no. 00-004-0802), whereas the pattern for Pt_{direct} exhibits distinct, sintered fcc Pt crystallites (Fig. 2A). These data are consistent with core-shell formation for $Pt_{C\text{-}S}$ but Pt phase-segregation for Pt_{direct}. In addition, $Pt_{C\text{-}S}$ showed a difference between the bulk and surface Pt:TiW ratios [28 versus 49%, as determined by inductively coupled plasma mass spectrometry (ICP MS) and x-ray photoelectron spectroscopy (XPS), respectively]. This surface ratio enhancement is indicative of Pt monolayers screening a TiW-rich core. In contrast, such surface screening was not observed for Pt_{direct}, where the bulk and surface Pt:TiW ratios were 20 and 18%, respectively.

Silica encapsulation prevented undesirable coking during carburization, as verified by a sixfold lower C-to-metal surface ratio for $Pt_{C\text{-}S}$ as compared to Pt_{direct} (Fig. 2B). Characteristic graphitic coke fibrils and sintered particles encapsulated in 4 to 5 nm of graphitic coke are visible in the TEM images of Pt_{direct} (Fig. 2C). In contrast, $Pt_{C\text{-}S}$ shows well-dispersed crystalline NPs with a uniform particle size distribution (PSD) of 6 to 8 nm and the absence of detectable coke layers. A heterometallic 27% $Pt_{0.67}Ru_{0.33}$/73% $Ti_{0.1}W_{0.9}C$ material (denoted $PtRu_{C\text{-}S}$) was synthesized analogously to $Pt_{C\text{-}S}$ (Fig. 2C and figs. S6 to S8). Although Ru could partition into the carbide core because it is less noble than Pt, STEM-EDX mapping (Fig. 2D) and XPS (fig. S7) indicate a core-shell structure with a Ru-enriched surface.

We compared the electrocatalytic properties of $Pt_{C\text{-}S}$ and $PtRu_{C\text{-}S}$ (8 wt% NM) to 20 wt% carbon-supported commercial (Premetek) electrocatalysts, denoted as Pt_{comm} and $PtRu_{comm}$, using gas diffusion electrodes (GDEs) (Fig. 3A) and rotating disk electrodes (RDEs) (Fig. 3, B to E). Carbon monoxide stripping voltammetry was used to determine the electrochemically active

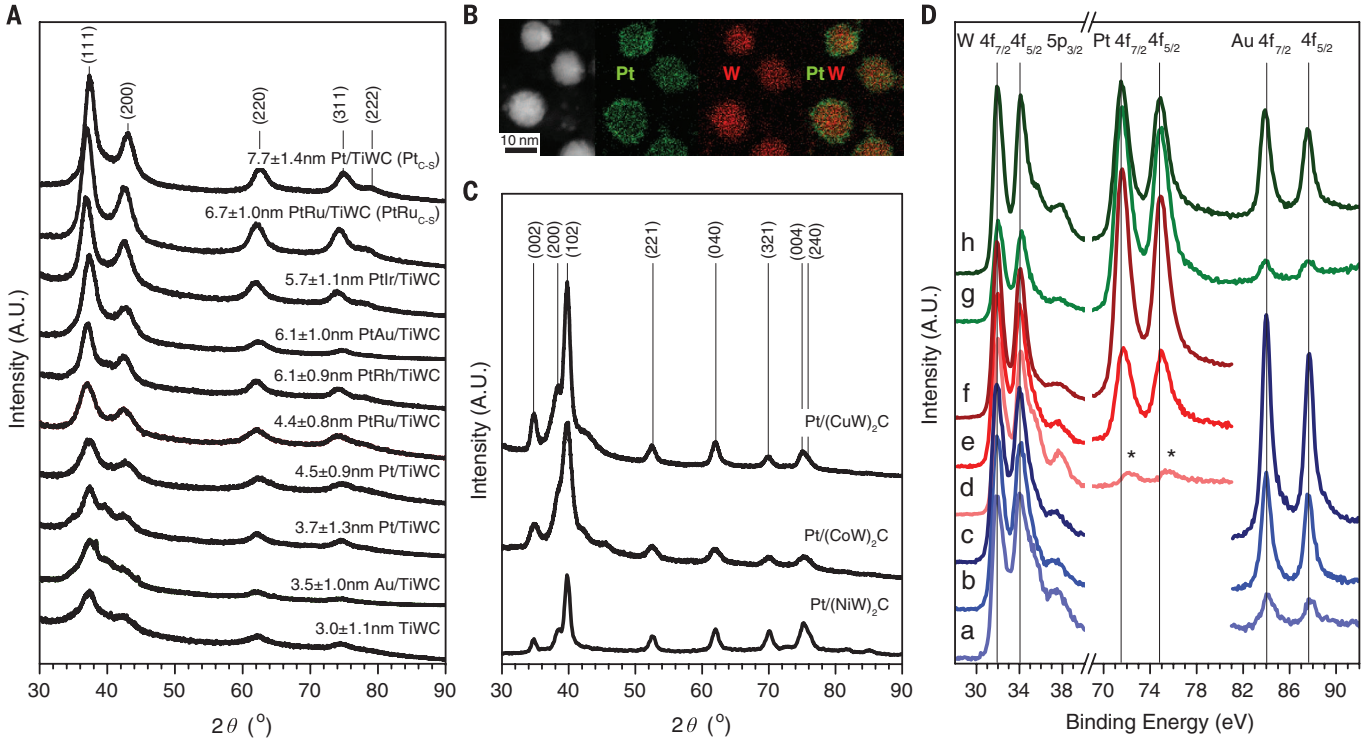

Fig. 4. Experimental exploration of various core-shell NM/TMC architectures. (**A**) PXRD diffractograms of NM/TiWC NPs of various sizes, compositions, and NM coverages. (**B**) STEM image and EDX maps of carbon-supported Pt/(CuW)$_2$C NPs. (**C**) PXRD diffractograms of Pt monolayers on various bimetallic semicarbide core NPs. (**D**) XPS spectra of (a to c) Au/TiWC NPs, (d to f) Pt/TiWC NPs, and (g and h) PtAu/TiWC NPs with submonolayer, monolayer, and multilayer NM shell thicknesses. The asterisks in (D) mark the Pt^{2+} signal.

surface area (CO-ECSA) and roughness factors of all materials (table S1 and fig. S9). Both Pt_{comm} and $PtRu_{comm}$ consist of 1- to 3-nm NPs (fig. S10) and have high CO-ECSAs of 68 ± 6 $m^2\ g^{-1}_{NM}$ and 99 ± 7 $m^2\ g^{-1}_{NM}$, respectively. Despite having larger PSDs (6 to 8 nm) than the commercial samples, both Pt_{C-S} and $PtRu_{C-S}$ achieved comparable CO-ECSAs of 50 ± 2 $m^2\ g^{-1}_{NM}$ and 73 ± 2 $m^2\ g^{-1}_{NM}$, respectively. Pt_{direct} did not exhibit a measureable CO-ECSA (fig. S9) and behaved analogously to carbon during cycling from 0.025 to 1 V (fig. S11).

The reactivity and stability of Pt_{C-S} and $PtRu_{C-S}$ were characterized by using density functional theory (DFT) and various probe reactions, including hydrogen evolution (HER), hydrogen oxidation (HOR), HOR under CO contamination, and methanol electrooxidation (MOR). Both Pt_{C-S} and $PtRu_{C-S}$ exhibited improved specific activity for HER and HOR, indicating that TiWC cores are excellent supports for NM monolayers and can favorably alter catalytic activity. Despite a 60% reduction in NM loading, Pt_{C-S} and $PtRu_{C-S}$ exhibited a symmetric activity profile during HER and HOR linear sweep voltammetry (LSV), similar to that for the commercial catalysts (Fig. 3A). Both core-shell materials exhibited HER and HOR Tafel slopes of ~30 mV dec^{-1} even after 10,000 cycles between −50 and 600 mV (table S2 and figs. S12 and S13). At an HER overpotential of 50 mV, both core-shell materials showed a fourfold improvement in specific activity and a threefold improvement in mass activity over the commercial catalysts (table S3) and maintained this enhancement after cycling.

Enhanced catalytic activity was corroborated by DFT calculations for thermally equilibrated Pt/TiWC slabs. Specifically, our calculations indicate Fermi level matching with Pt, which translates to minimal alterations to the work function of surface Pt by subsurface TiWC (*27*) (figs. S14 and S15), but show that the d-band center for a two-monolayer Pt shell downshifts from −2.7 to −2.8 eV (fig. S16). This downshift provides access to potentially favorable surface properties, such as a substantial weakening of the CO binding energy by ~40 kJ mol^{-1} (*28*). In turn, this effect can increase the tolerance of Pt_{C-S} and $PtRu_{C-S}$ toward CO poisoning, thereby overcoming a major challenge afflicting the performance of industrial Pt-based catalysts in many electrochemical applications (*11*, *28*).

Indeed, HOR experiments performed in the presence of high CO concentrations confirm that the TiWC cores mitigate poisoning on Pt and PtRu monolayers. Specifically, although 1000 parts per million of CO contamination markedly increased the HOR onset potential by ~400 mV for $PtRu_{comm}$ (Fig. 3B) and by ~200 mV for a state-of-the-art Pt/PtSn catalyst (*29*), both Pt_{C-S} and $PtRu_{C-S}$ catalyzed HOR with an overpotential as low as 50 mV. Under pure CO, both Pt_{C-S} and $PtRu_{C-S}$ achieved a ~200 mV lower onset potential and a 30-fold enhancement in specific activity for CO electrooxidation at 400 mV when compared to the commercial catalysts (fig. S17).

By decreasing the CO binding strength, the TiWC core is responsible for enhancing the MOR kinetics observed for Pt_{C-S} as compared to Pt_{comm}. The former features a higher specific activity over a wide potential window and a ~100 mV lower onset potential than Pt_{comm} (Fig. 3, C and D, and fig. S18). Ru is known to improve the MOR performance of Pt at low overpotentials via a bifunctional mechanism (*30*). Despite extensive efforts in the literature, little improvement in the activity and durability of MOR catalysts has been demonstrated over commercial PtRu/C in acidic media (*31*). Whereas both $PtRu_{C-S}$ and $PtRu_{comm}$ achieve a low onset potential of ~250 mV, $PtRu_{C-S}$ displays a higher steady-state turnover frequency (TOF) of 15.9 min^{-1} at 0.6 V as compared to 3.6 min^{-1} using $PtRu_{comm}$ (table S4), further evidencing the favorable activity modulation achievable using a TiWC core.

$PtRu_{C-S}$ also demonstrates enhanced stability as compared to $PtRu_{comm}$ (Fig. 3E and figs. S19 and S20). After 10,000 cycles, $PtRu_{comm}$ lost more than 50% of its steady-state activity at 0.35, 0.40, and 0.45 V, whereas the $PtRu_{C-S}$ activity decreased by only 35% at these potentials and actually improved at 0.6 V. A simple 2-min alkaline dip partially regenerated the activity of $PtRu_{C-S}$ at all potentials but had no appreciable benefit for $PtRu_{comm}$. Specifically, after regeneration, the overall loss in activity at 0.45 V was 18 and 55% for $PtRu_{C-S}$ and $PtRu_{comm}$, respectively. The final TOF at 0.6 V after 10,000 cycles and regeneration was 25.7 min^{-1} for $PtRu_{C-S}$, 2.4 min^{-1} for $PtRu_{comm}$, 1.8 min^{-1} for Pt_{C-S}, and 1.1 min^{-1} for Pt_{comm} (table S4), which represents an order of magnitude improvement of our core-shell material over the commercial catalysts.

No appreciable deactivation via particle sintering was observed for the core-shell materials after

10,000 cycles (Fig. 3F). HR-STEM and EDX mapping of $Pt_{C\text{-}S}$ after stability cycling show a highly crystalline composite NP with an intact Pt shell and a well-alloyed TiWC core (Fig. 3F and fig. S21). We attribute the improved stability of the core-shell materials to the strong NM-TMC interfacial bonds and to the lower surface free energies of large NPs relative to the surface free energies of ultrasmall NPs. These results demonstrate the ability of our method to reformulate a classic bimetallic NM catalyst, such as PtRu, into an architecture that preserves the complexity of the original bimetallic surface chemistry while favorably modulating catalytic performance through subsurface strain and ligand effects. As a class of materials that breaks the traditional metal-adsorbate scaling relations for transition metals (*32*), TMCs not only serve as promising core candidates to reduce NM loadings but could favorably affect catalytic activity for industrially relevant reactions, such as HOR, MOR, water-gas shift, or methanol synthesis, in which CO coverage effects deeply influence catalyst performance.

The high-temperature self-assembly process used here permits comprehensive control of the entire core-shell architecture for a variety of early and late transition metals (Fig. 4). Using TiWC cores, we synthesized NPs of controlled sizes (3 to 10 nm) with mono- and bimetallic shell compositions using mixtures of Ru, Rh, Ir, Pt, and Au (Fig. 4A and figs. S22 to S24). All materials crystallized into fcc WC lattices and displayed enhanced surface NM:TiW ratios, consistent with core-shell structures (figs. S25 to S27 and table S5). In addition, NM shells lattice-matched and self-assembled onto bimetallic semicarbide cores (PDF no. 00-020-1315) such as $(Cu_{0.2}W_{0.8})_2C$, $(Co_{0.2}W_{0.8})_2C$, and $(Ni_{0.3}W_{0.7})_2C$ (Fig. 4, B and C, and figs. S28 and S29). Although NM interfacial bond formation and stability were not explored on all possible TMC core formulations, our data suggest broader applicability of the method for synthesizing a variety of NM/TMC combinations.

For Au, Pt, and PtAu monolayers self-assembled on TiWC cores, the RME method also allowed control of the NM shell thickness from submonolayer [~0.5 monolayer (ML)] to multilayer (~3 ML) coverages (Fig. 4D). For each material, the extent of the XPS-determined surface NM:TiW ratio enhancement over the ICP-determined bulk NM:TiW ratio correlated with the monolayer coverage, ranging from 1 to 3% at submonolayer coverages to 10 to 20% screening at multilayer coverages (table S5). Unlike Au surfaces, the surface of Pt passivates under ambient conditions with a PtO layer, which is detectable as Pt^{2+} with XPS. As the monolayer coverage decreased for the Pt/TiWC system (Fig. 4D, spectra f to d), the Pt 4f signals shifted to higher binding energies, reaching 72.3 and 75.7 eV for the submonolayer sample (denoted as $Pt_{sub\text{-}ML}$). The presence of only PtO is consistent with submonolayer coverage, and such materials could have important applications in thermal catalysis, where both WC and Pt surface functionalities are accessible for catalytic transformations. When $Pt_{sub\text{-}ML}$ was supported on carbon and heated to 400° and 600°C in different atmospheres (H_2, dry N_2, or H_2O-saturated N_2), neither sintering nor discrete fcc Pt crystallites were detectable when using TEM and PXRD, and an enriched Pt:W ratio showing only Pt^{2+} surface species was observed with XPS (figs. S30 to S33). Collectively, TMC NPs coated with NM monolayers offer new, highly tunable pathways for decreasing NM loading requirements while increasing activity and stability in thermo- and electrocatalysis.

REFERENCES AND NOTES

1. A. T. Bell, *Science* **299**, 1688–1691 (2003).
2. G. A. Deluga, J. R. Salge, L. D. Schmidt, X. E. Verykios, *Science* **303**, 993–997 (2004).
3. J. Zhang, K. Sasaki, E. Sutter, R. R. Adzic, *Science* **315**, 220–222 (2007).
4. Y. Zhai *et al.*, *Science* **329**, 1633–1636 (2010).
5. L. Zhang *et al.*, *Science* **349**, 412–416 (2015).
6. C. Chen *et al.*, *Science* **343**, 1339–1343 (2014).
7. J. Greeley *et al.*, *Nat. Chem.* **1**, 552–556 (2009).
8. P. Strasser *et al.*, *Nat. Chem.* **2**, 454–460 (2010).
9. H. Yang, *Angew. Chem. Int. Ed.* **50**, 2674–2676 (2011).
10. F. Tao *et al.*, *Science* **322**, 932–934 (2008).
11. S. Alayoglu, A. U. Nilekar, M. Mavrikakis, B. Eichhorn, *Nat. Mater.* **7**, 333–338 (2008).
12. C. S. Bonifacio *et al.*, *Chem. Mater.* **27**, 6960–6968 (2015).
13. C. Cui, L. Gan, M. Heggen, S. Rudi, P. Strasser, *Nat. Mater.* **12**, 765–771 (2013).
14. C. Wang *et al.*, *Adv. Funct. Mater.* **21**, 147–152 (2011).
15. D. V. Esposito, J. G. Chen, *Energy Environ. Sci.* **4**, 3900–3912 (2011).
16. I. E. Stephens, A. S. Bondarenko, U. Grønbjerg, J. Rossmeisl, I. Chorkendorff, *Energy Environ. Sci.* **5**, 6744–6762 (2012).
17. J. A. Schaidle, N. M. Schweitzer, O. T. Ajenifujah, L. T. Thompson, *J. Catal.* **289**, 210–217 (2012).
18. S. T. Oyama, *The Chemistry of Transition Metal Carbides and Nitrides* (Blackie, Glasgow, 1996).
19. S. Ono, T. Kikegawa, Y. Ohishi, *Solid State Commun.* **133**, 55–59 (2005).
20. R. B. Levy, M. Boudart, *Science* **181**, 547–549 (1973).
21. L. H. Bennett, J. R. Cuthill, A. J. McAlister, N. E. Erickson, R. E. Watson, *Science* **184**, 563–565 (1974).
22. D. V. Esposito, S. T. Hunt, Y. C. Kimmel, J. G. Chen, *J. Am. Chem. Soc.* **134**, 3025–3033 (2012).
23. T. G. Kelly, A. L. Stottlemyer, H. Ren, J. G. Chen, *J. Phys. Chem. C* **115**, 6644–6650 (2011).
24. S. T. Hunt, T. Nimmanwudipong, Y. Román-Leshkov, *Angew. Chem. Int. Ed.* **53**, 5131–5136 (2014).
25. See the supporting materials on *Science* Online.
26. Y. C. Kimmel, X. Xu, W. Yu, X. Yang, J. G. Chen, *ACS Catal.* **4**, 1558–1562 (2014).
27. W. Schottky, *Annal. Physik* **362**, 541–567 (1918).
28. B. Hammer, Y. Morikawa, J. K. Nørskov, *Phys. Rev. Lett.* **76**, 2141–2144 (1996).
29. Z. Liu, G. S. Jackson, B. W. Eichhorn, *Angew. Chem. Int. Ed.* **49**, 3173–3176 (2010).
30. T. J. Schmidt, H. A. Gasteiger, R. J. Behm, *Electrochem. Commun.* **1**, 1–4 (1999).
31. A. K. Singh, Q. Xu, *ChemCatChem* **5**, 652–676 (2013).
32. R. Michalsky, Y. J. Zhang, A. J. Medford, A. A. Peterson, *J. Phys. Chem. C* **118**, 13026–13034 (2014).

ACKNOWLEDGMENTS

Work at MIT was supported by the U.S. Department of Energy, Office of Basic Energy Sciences (grant DE-FG02-12ER16352). This work used the Extreme Science and Engineering Discovery Environment (XSEDE), which is supported by the National Science Foundation (NSF) (grant ACI-1053575). The authors acknowledge the use of facilities and instrumentation supported by the University of Wisconsin Materials Research Science and Engineering Center (grant DMR-1121288). S.T.H. thanks NSF for financial support through the NSF Graduate Research Fellowship under grant no. 1122374. M.M. thanks the Swiss National Science Foundation (project number P2EZP2_159124) for financial support. J.A.D. acknowledges funding by the U.S. Department of Energy, Office of Basic Energy Sciences (grant DE-SC0014058).

SUPPLEMENTARY MATERIALS

www.sciencemag.org/content/352/6288/974/suppl/DC1
Materials and Methods
Figs. S1 to S33
Tables S1 to S5
References (*33*–*61*)

10 November 2015; accepted 15 April 2016
10.1126/science.aad8471

ROBOTICS

Perching and takeoff of a robotic insect on overhangs using switchable electrostatic adhesion

M. A. Graule,[1,2]* P. Chirarattananon,[2,3] S. B. Fuller,[2,4] N. T. Jafferis,[2] K. Y. Ma,[2] M. Spenko,[5] R. Kornbluh,[6] R. J. Wood[2]*

For aerial robots, maintaining a high vantage point for an extended time is crucial in many applications. However, available on-board power and mechanical fatigue constrain their flight time, especially for smaller, battery-powered aircraft. Perching on elevated structures is a biologically inspired approach to overcome these limitations. Previous perching robots have required specific material properties for the landing sites, such as surface asperities for spines, or ferromagnetism. We describe a switchable electroadhesive that enables controlled perching and detachment on nearly any material while requiring approximately three orders of magnitude less power than required to sustain flight. These electroadhesives are designed, characterized, and used to demonstrate a flying robotic insect able to robustly perch on a wide range of materials, including glass, wood, and a natural leaf.

Micro aerial vehicles (MAVs) with the capability to stay aloft for a prolonged time would be invaluable in many applications: providing a bird's-eye view of a disaster area, detecting hazardous chemical or biological agents, or enabling secure signal transmission in ad hoc communication networks. However, the flight time of aerial robots is restricted by the weight of their on-board power supplies and the lifetime of their mechanical components. Moreover, the endurance of current aerial robots decreases substantially as vehicle scale

Editor's Summary

Tough core-shell catalysts

One approach for increasing the activity of precious metals in catalysis is to coat them onto less expensive earth-abundant transition metal cores such as nickel, but often these structures alloy and deactivate during reactions. Hunt *et al.* synthesized several types of transition metal carbide nanoparticles coated with atomically thin precious-metal shells. Titanium-doped tungsten carbide nanoparticles with platinum-ruthenium shells were highly active for methanol electrooxidation, stable over 10,000 cycles, and resistant to CO deactivation.

Science, this issue p. 974